Journal of Materials Chemistry C

ROYAL SOCIETY OF CHEMISTRY

PAPER

View Article Online
View Journal

Cite this: DOI: 10.1039/d6tc00750c

Solid-state supramolecular assembly, luminescence thermometry and solution-state photoisomerization studies in lanthanide polyoxazamacrocycle†

Dominika Prętka, *[a] Przemysław Woźny, [a] Maciej Kubicki, [a] Marcin Runowski, [a] Violetta Patroniak, [a] Giuseppe Consiglio, [b] Giuseppe Forte [c] and Adam Gorczyński *[a]

Macrocyclic ligands provide a modular platform for luminescent lanthanide materials, yet predictive control over supramolecular nuclearity and functional response remains challenging. Here, we study a family of polyoxazamacrocycles bearing phenolate-based pendant arms – phenol (**LA_2H_2**), 3-ethoxy-phenol (**LB_2H_2**) and 4-(phenylazo)phenol (**LC_2H_2**) – and assess how pendant-arm identity and lanthanide ion (Dy^{3+}, Nd^{3+}) influence supramolecular assembly and photophysical behaviour. All metal ion/ligand combinations form inseparable mixtures of predominantly monometallic 1+1 species, nevertheless, the presence of dimetallic 2+2 species cannot be excluded. The assemblies adopt eight- or nine-coordinate lanthanide environments linked by macrocyclic donors, bound solvent and phenolate bridges, while lanthanide contraction does not dictate nuclearity, highlighting the intrinsic ambivalence of the N_3O_2/phenolate motif toward monomer–dimer outcomes. Semiempirical and DFT-level calculations provide insight into the multidimentional energy landscape of the macrocycle and coherent thermodynamic explanation for the coexistence of the 1:1 and 2:2 motifs. Despite such structural heterogeneity, functional solid-state lumienscence thermometry is realized through ligand–metal selection. All **LA_2**- and **LB_2**-based Nd^{3+} and Dy^{3+} complexes exhibit solid-state lanthanide-centered emission, with Nd/**LA_2** and Dy/**LB_2** enabling reliable intensity-ratio thermometry in near-infrared and visible-range, respectively. By contrast, azophenol-functionalized Ln/**LC_2** complexes exhibit photoresponsive behaviour exclusively in solution. Guided by design principles established in our earlier published six-membered macrocyclic systems, we assess here the transferability of azobenzene-based photoswitching to a five-donor polyoxazamacrocyclic scaffold. UV excitation induces azobenzene isomerization with partial, acid/base-gated reversibility, while no detectable solid-state emission is observed for these complexes, which indicates that solution-phase photoresponse is tolerant to nuclearity ambiguity but sensitive to macrocyclic framework and excitation window. Together, these observations benchmark the transferability of pendant-arm design strategies across lanthanide macrocyclic platforms.

Received 9th March 2026,
Accepted 22nd April 2026

DOI: 10.1039/d6tc00750c

rsc.li/materials-c

1. Introduction

Lanthanide-containing macrocyclic coordination compounds continue to attract intense interest as their properties emerge from the cooperative interplay of the organic host and the metal center, enabling multifunctional behaviour, diverse coordination modes and tunable physicochemical responses.[1–7] Macrocycles are typically accessed through covalent synthesis, dynamic covalent chemistry, or noncovalent self-assembly, yet all of these routes can suffer from modest ring-closing efficiencies.[8] High-dilution protocols and template-directed strategies have therefore been developed to favor cyclization, with metal ions, counter-anions, and even solvent molecules serving as structure-directing elements.[9–15] Despite these advances, lanthanide complexes remain challenging to control: pH, temperature and solvent can steer speciation, while the high coordination numbers and adaptable geometries of Ln^{3+} cations frequently lead to mono- *versus* polymetallic ensembles and coordination polymorphism.[16–18] The outstanding optical and magnetic

[a] *Faculty of Chemistry, Adam Mickiewicz University in Poznań, Uniwersytetu Poznańskiego 8, 61-614 Poznań, Poland. E-mail: adam.gorczynski@amu.edu.pl*
[b] *Department of Chemical Science University of Catania, Via S. Sofia 64, Italy*
[c] *Department of Drug Science and Health University of Catania, Via S. Sofia 64, Italy*

† Dedicated to Professor Bogdan Marciniec on the occasion of his 85th birthday.

attributes of rare-earth ions – sharp f–f bands, long excited-state lifetimes, magnetic anisotropy and photostability[19–25] – have propelled macrocyclic Ln^{3+} assemblies into applications spanning chemosensing, bioimaging and MRI contrast, optoelectronics, anti-counterfeiting and data storage.[26–41] In particular, luminescence thermometry – non-contact readout of temperature with high sensitivity – has emerged as quickly growing area in which coordination complexes are attractive because their emission can be rationally tuned through primary and secondary coordination-sphere design.[42–47] Macrocyclic platforms further offer chemical and thermal robustness along with geometry-dependent energy-transfer pathways that can impart reversible thermo-responsive behaviour.[48–53] Key determinants of emissive performance include the ligand skeleton and donor set, substituent electronics, secondary-sphere effects *e.g.,* coordinating solvents or counter-anions, noncovalent interactions *e.g.*, hydrogen bonding, and the identity of the Ln^{3+} ion, all of which govern sensitization efficiency, quenching channels and temperature dependences.[47–57]

Macrocycles derived from 2,6-diformylphenol commonly incorporate phenolic oxygen donors into the ring framework, yet phenolic pendant-arm designs remain comparatively rare.[4,5,10,58,59] Various derivatives of phenolic units can modulate the electronic interactions between the ligand and the metal center allowing for efficient emission from the lanthanide(III) ion. Thus, introduction of phenolic groups can significantly improve optical responses of designing Ln^{3+} complexes, because of its light-harvesting character, which influences the enhancement of the antenna effect by absorbing and transferring excitation energy to Ln^{3+} ion. Moreover, negatively charged phenolic units have a huge impact on coordination geometry around the metal centres, like influence on coordination numbers, coordination of additional molecules, ligand skeleton conformational preferences and its flexibility, proton-responsive behaviour, which are essential aspects of tuning optical or magnetic properties.[60–64] For the symetric, di-substituted 15-membered polyoxaaza pyridine-based macrocycle (15-pyN_3O_2), prior studies have focused on the benzimidazol-2-yl-methyl,[65] 2-pyridylmethyl,[66, 67]acetate,[68] or pyridine-*N*-oxide[69] pendant-arms. While their coordination behaviour was studied mainly with d-block metal ions[65–68] (and in one case Ln^{3+})[67] and primarily for magnetic properties, phenolic pendant-arms have not been yet explored (Fig. 1).

Here we introduce a family of Nd^{3+} and Dy^{3+} complexes with polyoxaza macrocycles bearing a common N_3O_2 donor set and two phenolate pendant-arms of systematically varied structure – phenol $\mathbf{LA_2H_2}$, ethoxyphenol $\mathbf{LB_2H_2}$ and phenylazophenol $\mathbf{LC_2H_2}$. We investigate how metal-ion size and ligand electronics/geometry dictate self-assembly, solid-state photophysics and solution diazobenzene behaviour, including their final application in optical thermometry (Fig. 1). Spectroscopic and structural characterization reveal that ionic radius or substituent class do not have dominant effect on the structure formation, and that all assemblies form equilibriating mixtures of 1+1 (mononuclear) and 2+2 (dinuclear) metal:ligand complexes. We show emissive behaviour for Nd^{3+} (NIR) and Dy^{3+} (visible) systems, attribute differences to substituent-dependent antenna/energy-transfer pathways and coordination environment, and establish structure–property

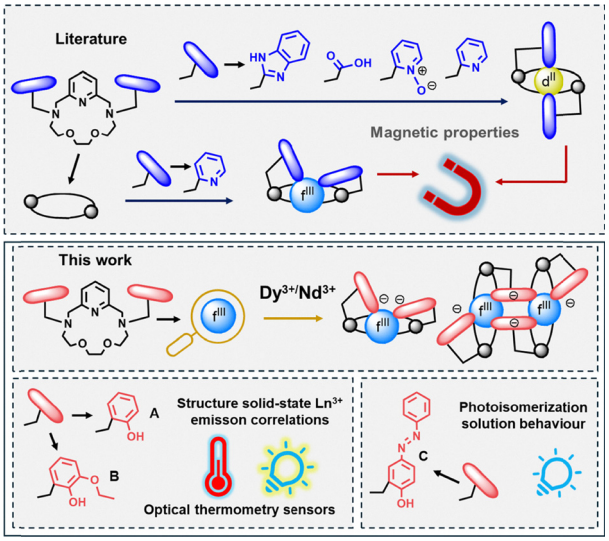

Fig. 1 Overview of the literature background and the studied macrocyclic ligand coordination with Ln^{3+} metal ions, highlighting structure-emission correlations and optical thermometry in the solid-state, alongside photo-switching behaviour in solution.

correlations relevant to molecular thermometry. Finally, using the azobenzene-based ligand $\mathbf{LC_2H_2}$, we probe photoisomerization in the free ligand and its Ln^{3+} complexes, clarifying how metal coordination and external stimuli regulate reversibility of the process. Together, these results expand pendant-phenolate macrocyclic chemistry to lanthanides, map the speciation landscape of 15-pyN_3O_2-type hosts and provide design rules for solid-state, temperature-responsive Ln^{3+} emitters.

2. Results and discussion

2.1. Design rationale

Macrocycles with tunable (1) ligand cavity size, (2) number and identity of donor atoms and (3) substituents on the ligand framework can coordinate various trivalent lanthanide ions to form thermodynamically robust complexes.[5,10] Predicting and controlling the resulting coordination motifs remains challenging, as the flexible high-coordination behaviour of Ln^{3+} ions often yields mono- *versus* polymetallic species, while lanthanide contraction and variable ligand stoichiometries complicate the outcome, further modulated by ligand identity, counterions and reaction parameters.[70–73] Numerous synthetic strategies address this speciation through judicious control of solvent, pH, temperature and templation, nevertheless, general design rules are still developing, underscoring the need for continued study.[10,17,18] Guided by these considerations, we targeted modular macrocyclic platforms whose structures can be systematically altered to probe structure–property relationships ion lanthanide photophysics (Fig. 2). Specifically, we selected a polyoxaaza, pyridine-containing macrocycle as a precursor for luminescent Ln^{3+} assemblies based on: (1) the established affinity of *O*/*N*-donor atoms for Ln^{3+} ions,[6,73,74] (2) the presence of N–H sites amenable to N-alkylation, thus enabling straightforward introduction of pendant groups,[75] and (3) the

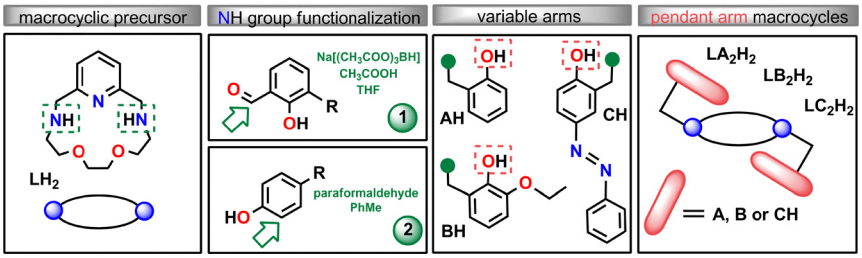

Fig. 2 Post-synthetic modification of macrocyclic precursor $\mathbf{LH_2}$ at the N–H sites to give symmetrically disubstituted macrocycles ($\mathbf{LA_2H_2}$, $\mathbf{LB_2H_2}$, $\mathbf{LC_2H_2}$) using two routes: reductive amination with aldehyde linkers (**AH**, **BH**) and a Mannich reaction with phenolic component (**CH**) and paraformaldehyde.

opportunity to tune ligand electronic structure *via* pendant-arm choice – a key factor for optimizing the antenna effect and maximizing energy transfer to the Ln^{3+} center.[76,77]

2.2. Strategies for ligand synthesis, its protonation- and ion-tiggered conformational changes

The polyoxaaza macrocycle precursor ($\mathbf{LH_2}$) was synthesized following the reported protocol,[78] by the Mg^{2+}-templated condensation of a pyridine dialdehyde with the corresponding diamine to promote macrocyclization, followed by demetallation and reduction of the C=N imine bonds (for full procedures and data see Experimental section, SI). Post-synthetic installation of symmetrical pendant-arms afforded three disubstituted macrocycles – $\mathbf{LA_2H_2}$, $\mathbf{LB_2H_2}$ and $\mathbf{LC_2H_2}$ – that differ in their aryl substituents (phenol, ethoxyphenol and phenylazophenol, respectively; Fig. 2). An aryl unit was chosen to provide a chromophore for antenna-based sensitization of Ln^{3+} emission,[77] while phenolic OH groups were incorporated as additional donor sites to reinforce coordination and support the higher coordination numbers characteristic of Ln^{3+} ions.[74]

Pendant-arm installation proceeded *via* N–H functionalization of $\mathbf{LH_2}$ (Fig. 2). While alkylation with halo-substituted reagents bearing amide, carboxylate or aryl groups is common for related scaffolds[28,65–68,75,79] we adopted two complementary routes here. Reductive amination of $\mathbf{LH_2}$ with commercially available aldehydes furnished $\mathbf{LA_2H_2}$ and $\mathbf{LB_2H_2}$ (conditions guided by the literature[80]), whereas a Mannich reaction between $\mathbf{LH_2}$ and a phenolic component and paraformaldehyde provided the azobenzene-bearing $\mathbf{LC_2H_2}$, mirroring successful symmetric functionalization of analogous diaza-crown macrocycles.[70] Complete synthetic schemes, together with characterization of intermediates and products, are compiled in Fig. S1–S8 and in Experimental section (SI). Under various synthetic/crystallization conditions – particularly in the presence of acids or bases – the ligands displayed protonation and ion-pairing at the macrocyclic nitrogens to give isolable salts (*e.g.*, $[NH]^+Cl^-$, $[NH]^+CF_3SO_3^-$), or adducts with small cations (*e.g.*, Na^+). Single-crystal X-ray diffraction (X-ray crystallography section, SI) confirms these formulations and reveals conformational shifts of the macrocycle upon protonation/ion binding that are informative for subsequent coordination design (structures summarized in Fig. S1–S8; additional spectroscopic data in Fig. S9 and S20).

2.3. Synthesis of lanthanide complexes and solution characterization

Complexes were obtained by combining 1.0 equivalent of ligand ($\mathbf{LA_2H_2}$, $\mathbf{LB_2H_2}$ or $\mathbf{LC_2H_2}$) with 1.0 equivalent of $Ln(OTf)_3$ (Dy or Nd) in CH_3CN, in the presence of 2.0 equivalents of Et_3N to generate the coordinating phenolate donors (see Experimental section, SI). FT-IR signatures diagnostic of coordination – together with close agreement between Nd^{3+} and Dy^{3+} series – indicate high isostructurality across metal ions and pendant-arm variants (Fig. S18–S20). MS analyses show that, under these conditions, the systems form equilibriating mixtures of 1:1 (mononuclear) and 2:2 (dinuclear) metal:ligand assemblies (Fig. 3). In the ESI-MS, two dominant signals are observed: a major 1:1 species with 100% relative intensity that is consistent with single Ln^{3+} bound to a doubly deprotonated ligand, and a minor 2:2 species (*ca.* 5% relative intensity) assigned to a dimeric assembly featuring two ligands and two metals, plausibly stabilized by μ-phenolate *O*-bridging between Ln^{3+} centers (Fig. S21–S28). The distribution thus favours monometallic 1:1 complexes under our standard conditions, while revealing intrinsic propensity for higher nuclearity consistent with the high coordination demands of Ln^{3+} ions, as further confirmed by X-ray analyses (see X-ray crystallography section, SI). Thus, generally, we denoted Ln-complexes, as Ln/$\mathbf{LX_2}$, where Ln (Nd^{3+} or Dy^{3+}), **X** (**A**, **B**, **C**), where the speciation to $\mathbf{LnLX_2}$ and $Ln_2(\mathbf{LX_2})_2$ is present. Conformational changes are also observed here in the context of metal-free systems as well as in the presence of sodium ions or protonated salts (Fig. S29).

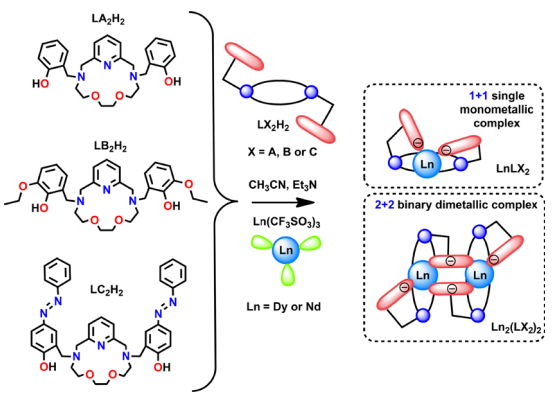

Fig. 3 Schematic representation of the synthesis and formation of 1+1 and 2+2 lanthanide macrocyclic complexes.

To probe complex formation in solution-state, we recorded ^{1}H NMR spectra for diamagnetic La^{3+} assemblies generated *in situ* by mixing $\mathbf{LB_2H_2}$ with $La(OTf)_3$ in CD_3CN and Et_3N (to deprotonate the phenols), with and without added urea as a neutral *O*-donor (Fig. S30a). For comparison, spectra of isolated La^{3+} complexes obtained *via* the standard precipitation workup were also acquired (see Experimental section, SI).

Across all conditions, the spectra are highly similar, indicating that the *in situ*-formed Ln^{3+}-macrocycle adducts correspond to those isolated from bulk synthesis and that the system rapidly approaches a thermodynamic equilibrium. Neither temperature increase, extended reaction time, nor addition of urea produced significant spectral changes. Notably, partial signal duplication in several regions is consistently observed, supporting the presence of more than one species in solution (and in the solids), most plausibly a mixture of mono- and dinuclear assemblies, in line with our structural and analytical assignments. To gain insight into the role of ionic radius, we compared La^{3+} with the smaller Lu^{3+} under analogous conditions. ESI-MS collected directly from the *in situ* mixtures (Fig. S30b and c) shows similar mono/di signals for both La^{3+} and Lu^{3+} mixtures. However, because dimeric Ln^{3+} assemblies can partially dissociate to monometallic ions under ESI conditions, these distributions cannot be taken as definitive speciation. In contrast, the ^{1}H NMR spectrum for Lu^{3+} is notably less complex than for La^{3+}, which most plausibly indicates a greater predominance of mononuclear species for the smaller Lu^{3+} ion, whereas La^{3+} retains a clearer mono/di mixture. Overall, the equilibrated mono/di manifold is radius-tunable: weakly perturbed for $Nd^{3+} \rightarrow Dy^{3+}$, but decisively biased at the extremes (La → Lu), where contraction stabilizes lower-nuclearity solutions without altering the fundamental coordination motifs. We emphasize that this interpretation remains tentative: beyond possible ESI-induced dissociation, we cannot exclude contributions from *syn*/*anti* stereoisomers analogous to those observed previously in 6-membered macrocyclic related systems.[81]

2.4. Solid-state structural analysis: predominant phase and thermodynamic equilibrium

To unambiguously determine structures of syntheiszed complexes, attempts to grow single crystals were made. Comprehensive crystallographic metrics are compiled in the SI (X-ray crystallography section); crystal/data-collection/refinement parameters are in Tables S1–S3 and selected geometry/conformational data in Tables S4 and S5. As suggested by solution studies, we envisage that solid-state assemblies can lead to systems with 1:1 M:L ratio, but mono *vs.* dimetallic equilibria might be present in the system. Single-crystal X-ray diffraction across the ligand series ($\mathbf{LA_2}$, $\mathbf{LB_2}$, $\mathbf{LC_2}$; ligands written without $\mathbf{H_2}$ to reflect phenolate deprotonation upon binding) reveals two recurring architectures: monometallic 1:1 complexes and dimetallic 2:2 assemblies. In the 1:1 form, the lanthanide is eight-coordinate (CN = 8): the macrocycle donates N_3O_2 from the ring plus two phenolate *O*-donors from the pendant-arms, and a neutral *O*-donor (H_2O, DMSO or urea) occupies the eighth site. In the 2:2 form, each metal retains the macrocycle's N_3O_2 set and phenolate donors, with two phenolates bridging the two metals and, depending on the system, an additional OH^- or neutral *O*-donor completing a nine-coordinate (CN = 9) environment at each Ln^{3+} center (Fig. 4). Dimeric sets in the case of $\mathbf{LA_2}$ based systems, essentially lead to monometallic species, since asymmetric unit is doubled into the structure of the dimetallic complex (Fig. 4i and j). The 15-membered polyoxaaza ring is conformationally versatile (compare also with semiempirical and DFT-level calculations at the end of this Section). Relevant torsion angles and intra-ring heteroatom distances (Table S4) show no simple correlation between ring conformation and speciation (free/protonated/mono- or dinuclear), consistent with a shallow conformational landscape that accommodates both CN = 8 and CN = 9 coordination. Crystal packing is supported by often disordered counter-ions and co-crystallized solvents, which establish hydrogen-bonded networks that stabilize the complexes (Fig. S29). Unless otherwise stated, discussion is limited to the primary coordination sphere; outer-sphere species are fully reported in the SI (see Tables S1–S3).

Across ligands, parallel speciation is observed – even under identical slow-diffusion conditions – confirming that each Ln/ligand pair can yield both 1:1 and 2:2 products (Fig. 4). For $\mathbf{LC_2}$, we obtained $Dy\mathbf{LC_2}(H_2O)$ (CN = 8; N_3O_2 + 2*O*(PhO^-) + H_2O) and $Dy_2(\mathbf{LC_2})_2(OH^-)$/$Nd_2(\mathbf{LC_2})_2(OH^-)$ (CN = 9; μ-phenolate + μ-OH^- bridging). For $\mathbf{LA_2}$, $Dy\mathbf{LA_2}(H_2O)$ mirrors the $\mathbf{LC_2}$ mononuclear coordination (CN = 8), while $Nd_2(\mathbf{LA_2})_2(H_2O)_2$ achieves CN = 9 *via* two μ-phenolates but no OH^- bridging; instead, one aqua per metal completes the inner sphere. For $\mathbf{LB_2}$, crystallization problems with oily products were overcome by slow evaporation from DMSO, affording $Dy\mathbf{LB_2}$(DMSO) (CN = 8; DMSO *O*-bound). Guided by this, introducing urea during complexation yielded $Dy\mathbf{LB_2}$(urea) and $Nd\mathbf{LB_2}$(urea), both 1:1, CN = 8 with urea as the neutral donor. Thus, mononuclear complexes consistently feature *N*/*O* donors from the macrocycle plus two phenolates and a neutral *O*-donor, whereas dinuclear complexes employ μ-phenolate bridging (±μ-*O*) to reach CN = 9. Finally, while lanthanide contraction (Nd^{3+} larger *vs.* Dy^{3+} smaller) could, in principle, bias coordination number or bridging mode, the present data show no systematic change in CN or bridging pattern between Nd^{3+} and Dy^{3+} under our conditions. Speciation is instead governed primarily by the phenolate-rich inner sphere and availability of auxiliary *O*-donors, reflecting the high coordination demands and strong Ln^{3+}–*O* affinity intrinsic to this ligand family (see Tables S1–S5 for comparative metrics).

To transition from liquid-phase to the solid state and check homogeneity and purity of the powders for luminescence studies, PXRD analyses were performed. For Dy/$\mathbf{LB_2}$ complex, the experimental PXRD pattern reflects with simulated pattern from theoretically optimized structure of monometallic $Dy\mathbf{LB_2}$(urea) crystals (Fig. S31). Importantly, for the related Dy/$\mathbf{LC_2}$ system, obtained mono- and dimetallic crystal structures allowed us to determine that these complexes exhibit clearly distinct theoretical PXRD fingerprints (Fig. S32). This indicates that changes in nuclearity of the complexes lead to differences in the solid-state arrangement. On this basis, demonstrated PXRD data Dy/$\mathbf{LB_2}$ complex (further investigated as luminescent thermometer)

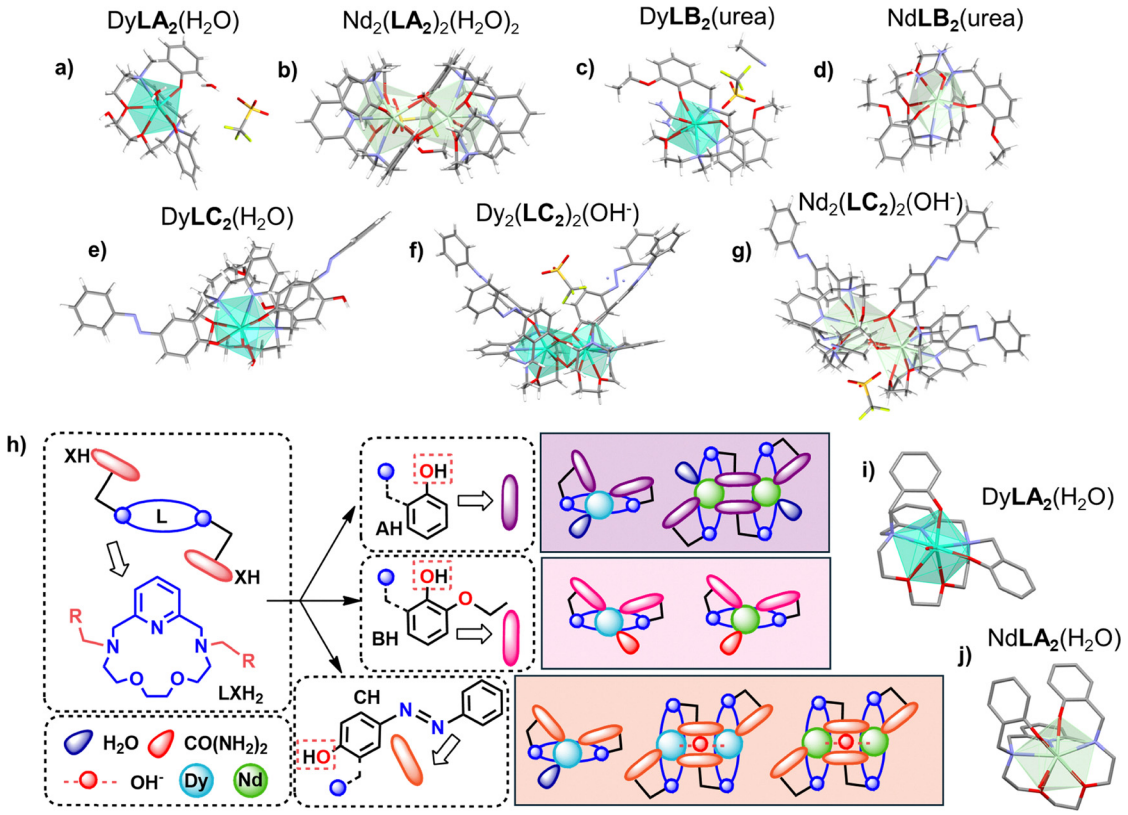

Fig. 4 X-ray crystal structures of Ln-macrocyclic complexes (a–g). Schematic representation of formation of 1+1 (mononuclear) and 2+2 (dinuclear) Ln-macrocyclic complexes with Dy^{3+} and Nd^{3+} ions, showing coordination-sphere schematics (h). All phenolic pendant-arms are deprotonated (phenolate); counter-ions are omitted. Asymmetric units of Dy**LA**$_2$(H$_2$O) and Nd$_2$(**LA**$_2$)$_2$(H$_2$O)$_2$ complexes (i and j).

strongly suggests that the monometallic complex represents the predominant crystalline phase in the bulk sample. In contrast, obtained Nd/**LA**$_2$ complex as amorphous powder does not exhibit long-range structural order, as evidenced by the absence of distinct diffraction peaks in the PXRD pattern. To check the homogeneity of the Ln/**LA**$_2$ system, the comparison of theoretical PXRD pattern for Dy**LA**$_2$(H$_2$O) crystals and experimental PXRD pattern for the Dy/**LA**$_2$ bulk sample analogous to the obtained bulk sample of Nd/**LA**$_2$ complex were investigated (Fig. S33). This comparison was possible, as the investigation of simulated PXRD patterns for crystals of dimetallic Ln$_2$(**LC**$_2$)$_2$ systems, confirms high isostructurality even the metal ions is changed from Dy^{3+} to Nd^{3+} (Fig. S32). This is plausibly due to the dimeric assembly being a doubled asymmetric unit of the complex (Fig. 4i and j). Here, when urea molecule is not introduced to the Ln^{3+} complex, main peaks observed in the experimental PXRD pattern generally match the theoretical spectrum of a monometallic complex, but problems with the crystallinity of the sample make diffraction peaks hard to compare, because of its intensity (Fig. S33). Despite the absence of enough crystalline of the samples based on **LA**$_2$ and **LC**$_2$ to confirm the high homogeneity of the samples, Ln^{3+} complexes were intentionally investigated as luminescent reference materials. The role was to evaluate the impact of different pendant-arms in the ligand skeleton on the observed emission behaviour, which may be another step forwards the rational design of similar systems in terms of optical properties. Importantly, the crystallinity of the sample was demonstrated to have no significant impact on the emission properties in the solid state. This conclusion is supported by the comparative luminescence measurements performed for the Dy/**LB**$_2$ complex, where the emission spectra of obtained powdered sample and crystalline material (for details, see experimental section, in SI) were found to be almost identical (Fig. S34). These results confirm that the observed emissive behaviour is controlled mainly by the local coordination environment rather than by long-range structural order. In conclusion, our comprehensive characterization demonstrates that in the solid samples the minor presence of dinuclear species does not dominate the overall structural and luminescent properties of the compounds investigated. The observed solid-state behaviour should be interpreted in the context of the intristic conformational flexibility of the macrocyclic skeleton.

To further support the above discussion and to gain insight into the intrinsic structural flexibility of the macrocyclic scaffold, the conformational landscape of the ligand was investigated through a combined conformational sampling and quantum mechanical refinement strategy. Three forms of the **LB**$_2$**H**$_2$ ligand were chosen, based on the X-ray structures: neutral, diprotonated ([**LH**$_2^{2+}$**B**$_2$**H**$_2$](CF$_3$SO$_3$)$_2$ triflate salt), and deprotonated (sodium Na**LA**$_2$**H**(CH$_3$OH) complex) forms. Extensive conformational sampling using CREST revealed a highly populated conformational space for all protonation states of the macrocycle. For the neutral,

protonated, and deprotonated systems, 802, 1233, and 854 conformers were identified, respectively. In all cases, the complete conformational ensemble was confined within an energy window of approximately 25 kJ mol^{-1}. The distribution of conformational energies is illustrated in the comparative energy distribution plot (Fig. S35a). The energy profiles show a continuous distribution of conformers across the entire energy range rather than a sharp clustering around a single global minimum. This behavior indicates the absence of a strongly dominant conformation and suggests that the macrocyclic framework possesses a shallow multidimensional potential energy surface. Further evidence of this behavior is provided by the cumulative energy distribution plot (Fig. S35b). The cumulative curves increase smoothly over the entire energy interval, indicating that numerous conformational states are accessible within a relatively narrow energy window. In contrast, a system dominated by a single well-defined minimum would exhibit a steep initial rise in the cumulative distribution followed by a plateau. The gradual increase observed here therefore reflects the presence of many closely spaced low-energy conformational minima. The nearly identical cumulative profiles obtained for the neutral, protonated, and deprotonated species further indicate that protonation has little influence on the intrinsic conformational flexibility of the macrocycle, suggesting that the shallow energy landscape is an inherent feature of the scaffold. To verify that this behavior persists at a higher level of theory, representative low-energy conformers extracted from the CREST ensembles were optimized using density functional theory. The resulting relative Gibbs free energies are summarized in Fig. S35c, which presents the corresponding energy ladder diagram. The calculations confirm that several conformers remain thermodynamically accessible in all protonation states. In the protonated system, the optimized structures are essentially isoenergetic, with relative free energies confined within approximately 2 kJ mol^{-1}, indicating near-degeneracy of the accessible conformations. The neutral system displays a somewhat broader distribution, extending to about 9 kJ mol^{-1}, while the deprotonated species shows the widest range, reaching roughly 17 kJ mol^{-1}. Nevertheless, even in these cases multiple geometrically distinct conformers remain within thermally accessible energy ranges, and no single conformation emerges as overwhelmingly dominant. Taken together, the conformational sampling and DFT refinement results demonstrate that the macrocyclic scaffold is characterized by a shallow and densely populated potential energy surface. The presence of numerous low-energy minima indicates a high degree of intrinsic structural plasticity. In such systems, relatively small perturbations – such as coordination to a metal center, interactions with counterions, or crystal packing effects – can stabilize different conformational basins of the underlying energy landscape. As a consequence, structurally distinct assemblies may arise from the stabilization of alternative low-energy conformations that already exist within the conformational manifold of the free ligand. Accordingly, experimental observations should be interpreted not as lack of purity, but as a manifestation of closely spaced thermodynamic minima inherent to the ligand architecture.

2.5. Luminescence and temperature-dependent properties of lanthanide complexes

The selected complexes were chosen for further investigation as luminescent temperature sensors, and their thermal stability was evaluated through thermogravimetric analysis (TGA) (Thermogravimetric analysis section, SI, Fig. S36 and S37). Solid-state luminescence studies were performed for all synthesized lanthanide complexes to investigate their photophysical properties, and the corresponding emission spectra are shown in Fig. S38. The observable emission of these systems from lanthanide ions depended precisely on the nature of the pendant-arms attached to the macrocycle. In complexes with the $\mathbf{LC_2}$ macrocycle (4-hydroxyazobenzene pendant-arms), the lanthanide emission is quenched, plausibly due to the quenching effects of the ligands and/or low energy of the triplet states, hampering effiecient energy transfer to the excited states of Ln^{3+} ions. While complexes with the $\mathbf{LA_2}$ and $\mathbf{LB_2}$ macrocycles (phenol or ethoxyphenol pendant-arms) showed lanthanide luminescence in the solid state. This observation highlighted the importance of structure–property relationships to observe efficient energy transfer to the Ln^{3+} centre and generate photoluminescence from lanthanide ions in these systems. Moreover, the type of lanthanide ion (Dy^{3+} *vs.* Nd^{3+}) strongly influences the emission intensity in complexes based on $\mathbf{LA_2}$ and $\mathbf{LB_2}$ macrocycles.

These findings emphasize that both the architecture of the ligand and the choice of metal centre are key factors in tuning the photophysical properties of lanthanide complexes and optimizing their performance as solid-state emissive materials. The most intensive emission of lanthanide ion was observed for Dy^{3+} complex with $\mathbf{LB_2}$ macrocycle and Nd^{3+} complex with $\mathbf{LA_2}$ macrocycle (Fig. 5a, b and Fig. S38). This is because the pendant-arms of the organic moieties modulate the energy transfer to the emitting lanthanide ions in the selected macrocyclic complexes.

The emission spectra for the $\mathbf{LA_2}$ and $\mathbf{LB_2}$ macrocyclic complexes with Nd^{3+} and Dy^{3+} ions were recorded at ambient conditions using LED-based UV light source (λ = 370 nm) for excitation. The $\mathbf{LA_2}$ complex with Nd^{3+} ions shows three characteristic emission bands in the range from 800 to 1100 nm, as a result of intraconfigurational, 4f–4f radiative transitions (Fig. 5a), namely a band at 820 nm ($^4F_{5/2} \rightarrow {}^4I_{9/2}$ transition), 890 nm ($^4F_{3/2} \rightarrow {}^4I_{9/2}$) and at 1050 nm ($^4F_{3/2} \rightarrow {}^4I_{11/2}$). On the other hand, the emission spectrum of the complex with Dy^{3+} shows seven disticts emission bands in the range of 450–780 nm, namely the bands centered at 455 nm ($^4I_{15/2} \rightarrow {}^6H_{15/2}$ transition), 480 nm ($^4F_{9/2} \rightarrow {}^6H_{15/2}$), 545 nm ($^4I_{15/2} \rightarrow {}^6H_{13/2}$), 580 nm ($^4F_{9/2} \rightarrow {}^6H_{13/2}$), 620 nm ($^4I_{15/2} \rightarrow {}^6H_{9/2}$), 665 nm ($^4F_{9/2} \rightarrow {}^6H_{9/2}$), and 755 nm ($^4F_{9/2} \rightarrow {}^6H_{7/2}$), as shown in Fig. 5b. The luminescence properties of both macrocyclic complexes are a result of initial UV excitation of the organic ligand, followed by the intersystem crossing (ISC) from the excited singlet (S_1) to triplet (T_1) state, the subsequent energy transfer (ET) from the excited triplet states of the organic ligands to the emitting lanthanide ions, and the final emission from their lowest excited states to the given ground levels, as presented in the energy level diagram in Fig. 5c. Specifically, after

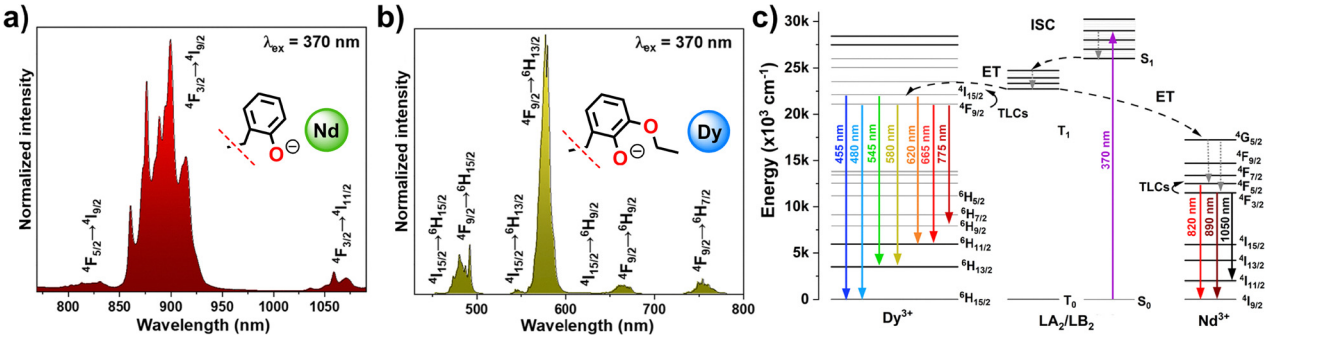

Fig. 5 Emission spectra of the macrocyclic complexes with Nd^{3+} (a) and Dy^{3+} ions (b) at ambient conditions recorded at 370 nm excitation. Energy level diagram showing the radiative and non-radiative processes in Nd/**LA**$_2$ and Dy/**LB**$_2$ based complexes (c).

the energy transfer to the higher excited states of Ln^{3+}, the non-radiative relaxation occurs to the lower-lying levels. In case of Dy^{3+} the lowest excited level is $^4F_{9/2}$, which is thermally-coupled with the $^6I_{15/2}$ level lying around 940 cm^{-1} above, causing emissions located in a visible range, ranging from 470 to 750 nm. In case when energy is transferred to Nd^{3+} ions, the non-radiative, multi-phonon relaxation occurs to the first excited state $^4F_{3/2}$, which is thermally-coupled with the $^4F_{5/2}$ excited level, lying around 1080 cm^{-1} above, leading to the emissions located in a NIR range, *i.e.* from 800 to 1100 nm. Such thermally-coupled levels (TCLs) are in thermal equilibrium and conform Boltzmann distribution, so they can undergo thermal excitation (Fig. 5c). For example, temperature elevation will cause intensification of Nd^{3+} emission at 820 nm (higher energy level), in the cost of decreasing emission intensity at 890 nm (lower energy level).

A detailed temperature-dependent analysis is presented in the following section. The temperature-dependent emission spectra of the Nd/**LA**$_2$ complex were investigated in the *T*-range from 90 to 540 K (Fig. 6a). In general, the normalized emission spectra show a relative increase in intensity of the high-energy emission band centered at 820 nm, which gradually increases with temperature, in respect to the low-energy band at 890 nm. This effect is caused by the mentioned thermalization effects between the TCLs of Nd^{3+}, *i.e.* $^4F_{3/2}$ and $^4F_{5/2}$ states. On the other hand, in the case of emission band centroids for peaks centered at 890 and 1050 nm (Fig. S39a and b), they show negligible, almost linear blueshift ($\Delta\lambda \approx -0.012$ and -0.006 nm K^{-1}, respectively). Moreover, their full width at half maximum (FWHM) increases with temperature elevation (Fig. S39c). By determining the integrated intensities of the mentioned bands, we calculated the luminescence intensity ratio (LIR) 820/890 nm, and plotted it as a function

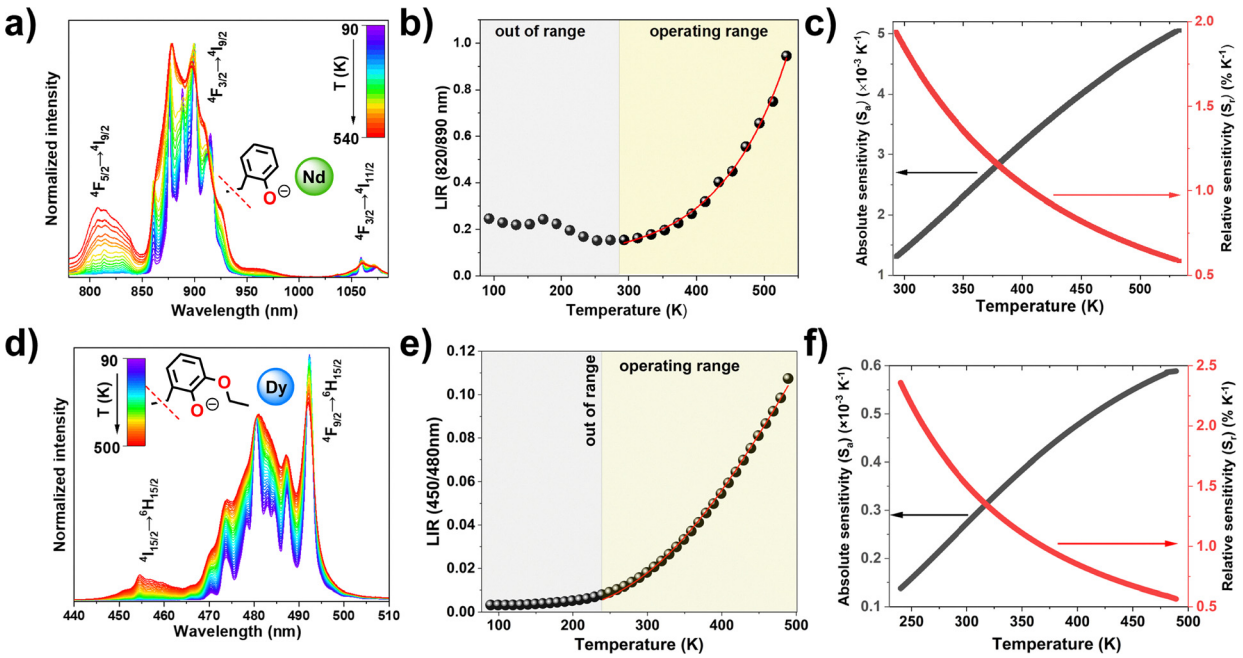

Fig. 6 Temperature-dependent emission spectra of the macrocyclic complex Nd/**LA**$_2$ (a) and Dy/**LB**$_2$ (d) ions. The determined LIR values for the thermalized emission bands of Nd/**LA**$_2$ (b) and Dy/**LB**$_2$ (e) complexes as a function of temperature. Absolute (left *y*-axis; black curve) and relative (right *y*-axis; red curve) sensitivity, calculated based on the 820/890 nm (c) and 450/480 nm (f) LIR parameters, for Nd^{3+} and Dy^{3+} complexes, respectively.

of temperature (Fig. 6b). Due to the very low intensity (close to the noise level) of the band at around 820 nm at low temperatures, and ineffective thermalization in the cryogenic *T*-range (deviations from the perfect Boltzmann-type distribution), the determined LIR values start to show a monotonic increasing tendency above 290 K (useful for thermometry operating range).

The resulting LIR values were fitted to the Boltzmann equation:

$$\mathrm{LIR} = \frac{I_1}{I_2} = B \times \exp\left(\frac{\Delta E}{k_B T}\right) \quad (1)$$

where B is 19.54 and ΔE is 1154 cm^{-1}. Using the LIR parameter as a function of temperature, the absolute sensitivity (S_a) was calculated using the following equation (eqn (2)):

$$S_a = \frac{\partial \mathrm{LIR}}{\partial T} \quad (2)$$

The S_a increases with temperature from $S_a \approx 1.29 \times 10^{-3}$ K^{-1} at 290 K to 5.06×10^{-3} K^{-1} at 540 K (Fig. 6c; left *y*-axis). However, in the case of the LIR factor, the most important thermometric parameter to estimate the performance of the temperature sensor is the relative sensitivity (S_r), which was calculated using eqn (3). The determined relative sensitivity decreases with temperature increase from 1.93% K^{-1} at 290 K to 0.57% K^{-1} at 540 K.

$$S_r = 100\% \frac{1}{\mathrm{LIR}} \left| \frac{\partial \mathrm{LIR}}{\partial T} \right|. \quad (3)$$

Next, the temperature-dependent emission properties of the **LB$_2$** complex with Dy^{3+} ions were investigated in the *T*-range from 90 to 490 K (Fig. 6d and Fig. S40). Luminescence intensities for all emission bands varied up to ~400 K, and then decreased as a function of temperature (Fig. S39d). However, the band at 450 nm show the relative increase of luminescence intensity, compared to the 480 nm band, due to thermalization effects between the $^4F_{9/2}$ and $^4I_{15/2}$ excited levels of Dy^{3+}, as can be clearly seen in the normalized spectra in Fig. 6d. A slight, monotonic blueshift of all band centroids (Fig. S39e) and apparent band broadening, *i.e.* FWHM increase (Fig. S39f), was observed for almost all emission bands as a function of temperature. We used the relative change in intensity for the bands located at 450 and 480 nm, corresponding to the $^4I_{15/2} \rightarrow {}^6H_{15/2}$ and $^4F_{9/2} \rightarrow {}^6H_{15/2}$ transitions, in order to determine the LIR 450/480 nm, as the most reliable thermometric parameter, which changes monotonically within a broad *T*-range. The LIR was fitted to the Boltzmann equation (eqn (1)), where B is 1.68 and ΔE is 946 cm^{-1}, showing effective thermalization of the $^4I_{15/2}$ level (Fig. 6e) above 200 K. The corresponding S_a parameter starts to increase from $\sim 1.38 \times 10^{-4}$ K^{-1} at ~240 K, where thermalization start to occur, up to 5.89×10^{-4} K^{11} at 490 K (Fig. 6f). In contrast, the S_r value decreases gradually from 2.36% K^{-1} at 200 K up to 0.56% K^{-1} at 490 K. Despite slightly smaller S_r, the Dy/**LB$_2$** macrocyclic complex shows the most promising spectroscopic and thermometric properties for optical temperature sensing, due to much higher luminescence intensity (Fig. S38), and monotonic change of the LIR parameter within a broader *T*-range than the Nd/**LA$_2$** complex, due to specific structure-related optical properties of the Dy^{3+}-based macrocycle compound with ethoxyphenol pendant-arms.

2.6. Photoresponsive behaviour in solution-state

The azobenzene unit is a well-known photoswicthable moiety capable of reversible *trans–cis* isomerization under light exctitation, in which characteristic absorption bands from these two isomers makes them distinguishable.[82] Here, we investigated the **LC$_2$H$_2$** ligand with azobenzene pendant-arms, as well as its lanthanide complexes – Nd/**LC$_2$** and Dy/**LC$_2$** complexes with the aim of studying their potential for light-responsive behaviour. Upon irradiation of the free ligand **LC$_2$H$_2$** within the range (315–500 nm) using selected wavelengths, noticeable spectral changes were observed (Fig. S41a). The most observable changes occurred upon irradiation of 360 nm, corresponding to the absorption maximum of the ligand. Additionally, evidence of isomerization was also detected upon irradiation at 405 nm. In both cases the spectra were almost recovered after 10 minutes of keeping irradiated sample in the dark. Nevertheless, the observed spectral changes did not induce photochromic behaviour of the system. Significant activity was observed however upon coordination with Nd^{3+} or Dy^{3+} lanthanide ions. Importantly, photoirradiation of lanthanide systems leads to enhanced stabilization of the *cis* isomer. This strongly indicates that coordination of Ln^{3+} metal ion plays an important role in photoresponsive and photochromic behaviour in these systems. Metal ion coordination through ligand skeleton and the negatively charged oxygen donors from phenolate moieties can impact the energetic profiles for the effective *trans*-to-*cis* isomerization. For the Nd/**LC$_2$** complex, a wavelength screening was performed in chloroform solution to determine the most efficient excitation range for photoisomerization. The results indicated efficient isomerization upon exposure to near-UV light at 270 nm. From 300 nm to 560 nm, no significant changes were observed in the absorption spectrum, indicating that isomerization at these wavelengths is not efficient (Fig. S41b). Irradiation at 270 nm led to decrease in the intensity of the *trans*-band (around 390 nm), accompanied by the appearance and growth of the *cis*-band (around 520 nm) – pink line, confirming the photoinduced isomerisation process (Fig. 7a and Fig. S41b). This behaviour is consistent with our previously published results on azobenzene containing lanthanide complexes based on a different macrocyclic skeleton, where photoresponse was tiggered by further UV region, and most of Ln^{3+} complexes, exhibited dual photoisomerization regions under both UV (320 nm) and visible light (520 nm) irradiation.[81] In those systems, the reverse *cis*-to-*trans* isomerization was induced by contact with glass surface. Similar observations were made in the present study, although the reversibility was notably reduced.

This potentially indicated partial degradation[83] in the chloroform solution of the lanthanide complex due to the high-energy UV light required for isomerisation activation, as spectra was no more recoverable, even after prolonged (24 hours) contact with the glass surface (Fig. 7a). Therefore, in the subsequent experiments, we employed irradiation at a slightly lower-energy wavelength (285 nm), which still proved effective for inducing isomerization and could minimaze degradation effects. We

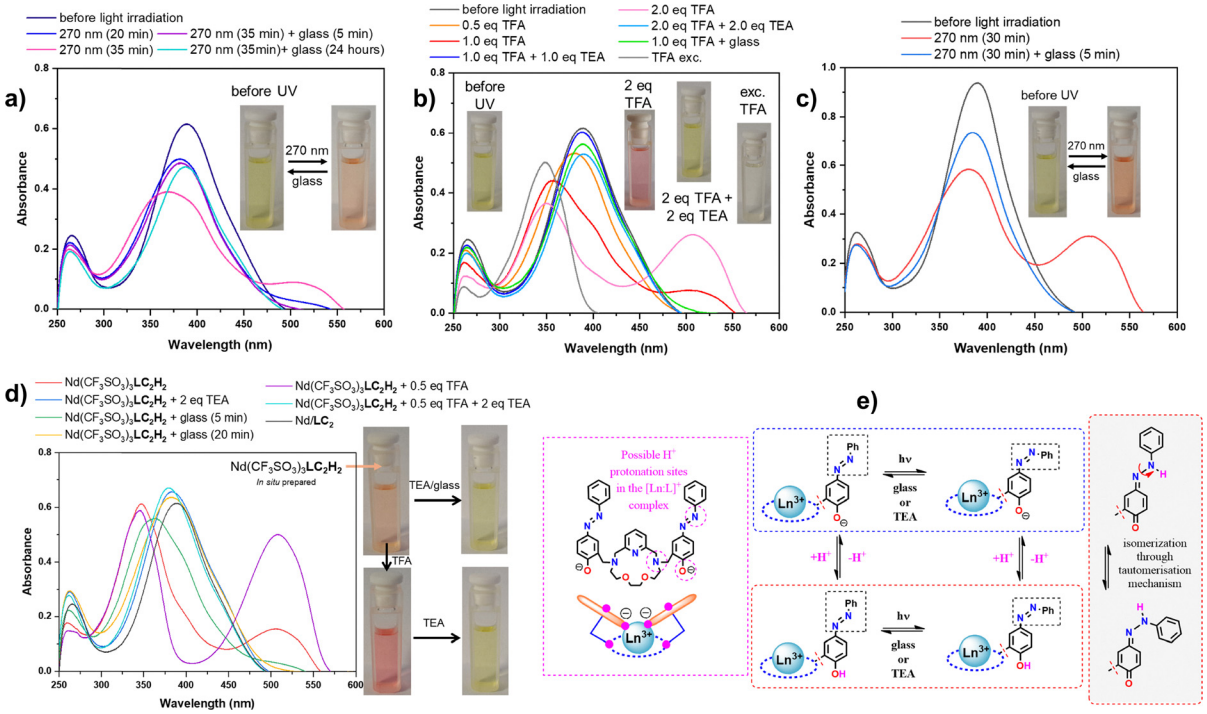

Fig. 7 UV-Vis absorption spectra changes for Nd/$\mathbf{LC_2}$ after contact with the glass, followed by irradiation at 270 nm (a), UV-Vis absorption spectra changes under defined conditions of Nd/$\mathbf{LC_2}$ lanthanide complex (acid–base equilibrium) (b), Dy/$\mathbf{LC_2}$ lanthanide complex after contact with the glass, followed by irradiation at 270 nm (c) and *in situ* prepared Nd$(CF_3SO_3)_3\mathbf{LC_2H_2}$ complex under defined conditions (d) with the comparison to the absorption spectra of deprotonated Nd/$\mathbf{LC_2}$ complex. The photos inserted into the graphs show specific changes in the colour of the solutions. Graphical representation of protonation and its effect on the photoresponsive behaviour of the macrocyclic lanthanide assemblies (e); for better demonstration of the process, the phenolic arm is presented as non-coordinating, but solution and solid-state studies demonstrate coordination in the deprotonated form; the mechanism is presented based on monometallic Ln-assemblies.

observed the same trends of changes in the absorption spectrum as at 270 nm. The *cis*-rich solution reached its maximum after 135 minutes of irradiation, as indicated by the lack of increasing intensity of the band assigned to the *cis*-isomer (Fig. S42a). The *cis*-rich solution was also irradiated with visible light (480 nm and 520 nm) to induce reversion to the *trans*-form, however it caused only a slight reversion in the *cis*-absorption band intensity. Leaving this sample for 24 hours in the day light, caused disappearance of characteristic band of the *cis*-isomer, whereas the sifted band assigned to the *trans*-isomer remains unchanged (Fig. S42a). This findings indicate that such prolonged irradiation with high-energy light may induce some degradation pathway, and that the process is no longer reversible, contrary to the 6-membered macrocyclic azobenzene/phenoxide system.[81] We also investigated the effect of acid and base addition on the isomerization process (Fig. 7b). We found that trifluoroacetic acid (TFA) favours the formation of the *cis*-isomer, accompanied by a colour change form yellow to orange, suggesting a mechanism based on a protonation/deprotonation equilibrium. Contact of this solution with borosilicate glass or addition of a base such a triethylamine (TEA), restores absorption spectra and the yellow colour of the solution. The reversibility is achieved with significantly higher efficiency than in the case of UV-induced photoisomerization. However, in the presence of excess of TFA, the *cis*-band disappears completely, and the process is no longer reversible, which may indicate metal ion decoordination (Fig. 7b). Analogous experiments with the Dy/$\mathbf{LC_2}$ complex confirmed similar behaviour. Efficient photoisomerization was observed at 270 nm, with partial reversibility upon contact with glass (Fig. 7c). However, as with the Nd/$\mathbf{LC_2}$ complex, reduced reversibility indicates sample fatigue or partial degradation under prolonged UV exposure. For Dy^{3+} based complex acid/base interactions again play an important role in modulating the *cis–trans* equilibrium (Fig. S42b). Furthermore, an *in situ* preparation of the Nd$(CF_3SO_3)_3\mathbf{LC_2H_2}$ complex without deprotonation of phenol groups, resulted in an immediate *cis*-like spectrum, which reverted after base addition (TEA) or upon contact with glass, however longer time was required – 20 minutes (Fig. 7d). Additionally, it is clearly visible that the addition of TFA as a protonating medium shifts the equilibrium further towards the *cis*-form, which is observed as a significant increase in the intensity of the absorption band around 500 nm. The entire process is also reversible upon introduction of TEA, and the resulting absorption spectrum matches the Nd/$\mathbf{LC_2}$ complex spectrum almost exactly (Fig. 7d). It should be noted that protonation of the ligand molecule ($\mathbf{LC_2H_2}$) by TFA addidtion (even with excess) does not induce the appearance of band in the Vis-region of the spectrum, which is typically assigned with the *cis*-form of azobenzene moiety, and thus not induce any colour change (Fig. S42c). This indicates that metal coordination plays a crucial role in designing such photoswitchable systems based on the skeleton on this azobenzene macrocycle. All studies

connected with the protonation and deprotonation behaviour influences the photostationary state on our Ln-systems. Thus, we hypothesize that protonation of the phenolic lariat arms can promotes intramolecular proton transfer to the azo group, generating a hydrazone-type tautomer in which the N–N single bond lowers the rotational barrier for the isomerization (Fig. 7e).

3. Conclusions

Across the polyoxaaza, pyridine-containing macrocycles studied here, two recurring architectures – 1:1 (monometallic) and 2:2 (dinuclear) – are obtained irrespective of the pendant-arm identity (**LA_2**, **LB_2**, **LC_2**) or mid-series ion size (Dy^{3+} *vs.* Nd^{3+}). This parallel speciation reflects the intrinsic coordination behaviour of the phenolate-rich macrocycle: the ring N_3O_2 donors enforce binding while phenolates promote μ-OH^-/μ-phenolate bridging and high effective coordination numbers. Solution NMR and ESI-MS indicate a thermodynamically equilibrated mono <=> di manifold, with lanthanide-radius effects modest for Nd^{3+}/Dy^{3+} but becoming more pronounced at the series limits (La → Lu), where smaller ions bias toward mononuclear solutions. The combined semiempirical and DFT-level computations further confirm the intrinsic conformational degeneracy across all protonation states of the macrocyclic scaffold, and a coherent thermodynamic explanation for the coexistence of 1:1 and 2:2 coordination motifs. Pendant-arm electronics govern emissive behaviour in the solid state: **LC_2** (azobenzene) quenches Ln^{3+} emission, whereas **LA_2** (phenol) and **LB_2** (ethoxyphenol) support efficient antenna-mediated sensitization, with Dy/**LB_2** and Nd/**LA_2** giving the robust luminescent output and reliable thermometric response, despite the observed 1:1/2:2 coexistence of complexes. In solution, azobenzene photoisomerization is coordination-enhanced (the free ligand is photoactive at a different wavelength and its *cis* form is less stable, whereas the Ln^{3+} complexes exhibit shifted absorption and significantly enhanced *cis* stability). Near-UV excitation triggers *trans* → *cis* conversion, while acid/base inputs offer a more reversible handle on the *cis–trans* balance, albeit with reduced reversibility under sustained high-energy irradiation or excess acid and overall inferior characteristics when compared with 6-donor analogues.[81] Together, these findings provide structure-guided rules for lanthanide macrocycle design within the 5-donor N_3O_2 ligand scaffolds. Tailoring pendant-arm electronics and managing the radius-sensitive mono/di equilibrium enable solid-state emitters and practical LIR-type thermometers. This integrated approach links ligand architecture through speciation and energy-transfer pathways, offering a clear route to multifunctional, responsive Ln^{3+} materials.

Author contributions

Dominika Prętka: conceptualization, methodology, data curation, investigation, visualization, writing – original draft, and writing – review & editing; Przemysław Woźny: data curation, investigation, and writing – original draft; Maciej Kubicki: data curation, formal analysis, visualization, and writing – original draft; Marcin Runowski: visualization, writing – review & editing, and resources; Violetta Patroniak: supervision, visualization, and writing – review & editing, funding acquisition; Giuseppe Consiglio: methodology, and writing – review & editing; Giuseppe Forte: formal analysis, methodology, and writing – review & editing; Adam Gorczyński: conceptualization, methodology, investigation, visualization, writing – original draft, writing – review & editing, project administration, supervision, resources, and funding acquisition.

Conflicts of interest

There are no conflicts to declare.

Data availability

The data supporting this article have been included as part of the supplementary information (SI) and are available in the public open repository Zenodo at https://zenodo.org/records/18130840; DOI: https://doi.org/10.5281/zenodo.18130840. Supplementary information is available. See DOI: https://doi.org/10.1039/d6tc00750c.

Acknowledgements

This work was supported by the National Science Centre, Poland grant no. 2022/47/B/ST4/02310 (PI: V. P.), 2020/39/D/ST4/01182 (PI: A. G.), and grant no. 2023/50/E/ST5/00021 (PI: M. R.).

References

1 S. J. Archibald, *Annu. Rep. Prog. Chem., Sect. A: Inorg. Chem.*, 2009, **105**, 297–322.
2 L. F. Lindoy, K.-M. Park and S. S. Lee, *Chem. Soc. Rev.*, 2013, **42**, 1713–1727.
3 J.-C. G. Bünzli, *J. Coord. Chem.*, 2014, **67**, 3706–3733.
4 C. A. Chang, in *Handbook on the Physics and Chemistry of Rare Earths*, ed. J.-C. G. Bünzli and V. K. Pecharsky, Elsevier, 2017, vol. 51, pp. 169–299.
5 K. Atal, U. Phageria, S. Kumari, Y. Dhayal and S. Bugalia, *Inorg. Chim. Acta*, 2024, **561**, 121857.
6 W. Radecka-Paryzek, V. Patroniak and J. Lisowski, *Coord. Chem. Rev.*, 2005, **249**, 2156–2175.
7 M. Rezaeivala and H. Keypour, *Coord. Chem. Rev.*, 2014, **280**, 203–253.
8 J. Yu, D. Qi and J. Li, *Commun. Chem.*, 2020, **3**, 189.
9 N. E. Borisova, M. D. Reshetova and Y. A. Ustynyuk, *Chem. Rev.*, 2007, **107**, 46–79.
10 V. Alexander, *Chem. Rev.*, 1995, **95**, 273–342.
11 N. V. A. Gerbeleu and V. B. Burgess, *Template Synthesis of Macrocyclic Compounds*, 1999, pp. 201–270.
12 C. M. Taylor and N. L. Kilah, *J. Incl. Phenom. Macrocycl. Chem.*, 2022, **102**, 543–555.

13 G. Klein, A. Llevot, P. Löser, B. Bitterer, J. Helfferich, W. Wenzel, C. Barner-Kowollik and M. A. R. Meier, *J. Incl. Phenom. Macrocycl. Chem.*, 2019, **95**, 119–134.
14 N. V. A. Gerbeleu and V. B. Burgess, *Template Synthesis of Macrocyclic Compounds*, 1999, pp. 1–27.
15 V. Martí-Centelles, M. D. Pandey, M. I. Burguete and S. V. Luis, *Chem. Rev.*, 2015, **115**, 8736–8834.
16 P. Guerriero, S. Tarnburini and P. A. Vigato, *Coord. Chem. Rev.*, 1995, **139**, 17–243.
17 X.-Z. Li, C.-B. Tian and Q.-F. Sun, *Chem. Rev.*, 2022, **122**, 6374–6458.
18 K.-H. Yim, C.-T. Yeung, H.-Y. Wong and G.-L. Law, *Inorg. Chem. Front.*, 2021, **8**, 2952–2964.
19 W.-L. Zhou, Y. Chen, W. Lin and Y. Liu, *Chem. Commun.*, 2021, **57**, 11443–11456.
20 X. Zhu, W.-K. Wong, W.-Y. Wong and X. Yang, *Eur. J. Inorg. Chem.*, 2011, 4651–4674.
21 E. Mathieu, S. R. Kiraev, D. Kovacs, J. A. L. Wells, M. Tomar, J. Andres and K. E. Borbas, *J. Am. Chem. Soc.*, 2022, **144**, 21056–21067.
22 S. Ullmann, P. Hahn, P. Mini, K. L. Tuck, A. Kahnt, B. Abel, M. E. Gutierrez Suburu, C. A. Strassert and B. Kersting, *Dalton Trans.*, 2020, **49**, 11179–11191.
23 M. E. Thornton, J. Hemsworth, S. Hay, P. Parkinson, S. Faulkner and L. S. Natrajan, *Front. Chem.*, 2023, **11**, 1232690.
24 K. Zhang, Z.-Y. Lu, C.-C. Feng, Z.-R. Yang, P.-P. Nie, T.-T. Chen, L.-F. Zhang, S. Ma, Y.-J. Shen and M.-L. Lin, *ACS Omega*, 2019, **4**, 18334–18341.
25 S. E. Bodman and S. J. Butler, *Chem. Sci.*, 2021, **12**, 2716–2734.
26 C. S. Bonnet and T. Gunnlaugsson, *New J. Chem.*, 2009, **33**, 1025–1030.
27 P. Mini, S. E. Walker, M. R. Grace, G. H. Dennison and K. L. Tuck, *Dalton Trans.*, 2023, **52**, 12235–12243.
28 G. Castro, G. Wang, T. Gambino, D. Esteban-Gómez, L. Valencia, G. Angelovski, C. Platas-Iglesias and P. Pérez-Lourido, *Inorg. Chem.*, 2021, **60**, 1902–1914.
29 R. E. Mewis and S. J. Archibald, *Coord. Chem. Rev.*, 2010, **254**, 1686–1712.
30 F. Oukhatar, S. V. Eliseeva, C. S. Bonnet, M. Placidi, N. K. Logothetis, S. Petoud, G. Angelovski and É. Tóth, *Inorg. Chem.*, 2019, **58**, 13619–13630.
31 Y. Tang, M. Jian, B. Tang, Z. Zhu, Z. Wang and Y. Liu, *Inorg. Chem. Front.*, 2024, **11**, 2039–2048.
32 A. J. Salazar-Medina, R. E. Navarro, H. Santacruz-Ortega, A. U. Orozco-Valencia, R. I. Lopéz-Esquivel, Y. Soberanes and C. J. Salas-Juárez, *Opt. Quantum Electron.*, 2024, **56**, 1064.
33 H. Yan, J.-L. Wang, H. Wang, H.-Q. Tian and W.-B. Sun, *Inorg. Chem. Front.*, 2025, **12**, 6655–6662.
34 S. Wang, T.-Z. Wu, H.-J. Park, T. Peng, L.-X. Cao, S. K. Mellerup, G.-Q. Yang, N. Wang and J.-B. Peng, *Adv. Opt. Mater.*, 2016, **4**, 1882–1892.
35 W.-L. Zhou, W. Lin, Y. Chen, X.-Y. Dai and Y. Liu, *Small*, 2023, **19**, 2304009.
36 Y. Gil, A. Castro-Alvarez, P. Fuentealba, E. Spodine and D. Aravena, *Chem. – Eur. J.*, 2022, **28**, e202200336.
37 A. Homberg, F. Navazio, A. Le Tellier, F. Zinna, A. Fürstenberg, C. Besnard, L. Di Bari and J. Lacour, *Dalton Trans.*, 2022, **51**, 16479–16485.
38 P.-Y. Liao, Y. Liu, Z.-Y. Ruan, H.-L. Wang, C.-G. Shi, W. Deng, S.-G. Wu, J.-H. Jia and M.-L. Tong, *Inorg. Chem.*, 2023, **62**, 1075–1085.
39 B. Zhang, X. Guo, P. Tan, W. Lv, X. Bai, Y. Zhou, A. Yuan, L. Chen, D. Liu, H.-H. Cui, R. Wang and X.-T. Chen, *Inorg. Chem.*, 2022, **61**, 19726–19734.
40 M. Costanzo, S. Bianco, M. Fik-Jaskółka and G. N. Roviello, *Int. J. Mol. Sci.*, 2026, **27**, 1566.
41 E. Ewert, D. Marcinkowski, I. Pospieszna-Markiewicz, R. Palumbo, Z. Hnatejko, M. Kubicki, A. Gorczyński, E. Wieczorek-Szweda, V. Patroniak, G. N. Roviello and M. Fik-Jaskółka, *Int. J. Biol. Macromol.*, 2025, **330**, 148269.
42 M. Runowski, P. Woźny, N. Stopikowska, I. R. Martín, V. Lavín and S. Lis, *ACS Appl. Mater. Interfaces*, 2020, **12**, 43933–43941.
43 C. Hernández-Álvarez, P. I. Martín-Hernández, I. R. Martín, F. Rivera-López, H. Hemmerich, M. Grzegorczyk, S. Mahlik and M. Runowski, *Adv. Opt. Mater.*, 2024, **12**, 2303328.
44 C. D. S. Brites, S. Balabhadra and L. D. Carlos, *Adv. Opt. Mater.*, 2019, **7**, 1801239.
45 C. D. S. Brites, R. Marin, M. Suta, A. N. Carneiro Neto, E. Ximendes, D. Jaque and L. D. Carlos, *Adv. Mater.*, 2023, **35**, 2302749.
46 R. Li, F.-F. Xu, Z.-L. Gong and Y.-W. Zhong, *Inorg. Chem. Front.*, 2020, **7**, 3258–3281.
47 Y. Hasegawa and Y. Kitagawa, *J. Mater. Chem.*, 2019, **7**, 7494–7511.
48 D. Marcinkowski, D. Prętka, P. Woźny, J. Kobylarczyk, A. Siwiak, D. Pakulski, V. Patroniak, K. Roszak, A. Katrusiak, R. Herchel, R. Podgajny, S. Sobczak, N. Majewska, S. Mahlik, M. Runowski and A. Gorczyński, *Adv. Opt. Mater.*, 2025, **13**, 2500495.
49 Y. Ning, Y.-W. Liu, Y.-S. Meng and J.-L. Zhang, *Inorg. Chem.*, 2018, **57**, 1332–1341.
50 P. Gawryszewska, K. Ślepokura and J. Lisowski, *Inorg. Chem.*, 2024, **63**, 15875–15887.
51 P. Fuentealba, D. Villagra, Y. Gil, H. Aguilar-Bolados, R. Costa de Santana, G. Gasparotto, A. Vega, J. Manzur and E. Spodine, *Eur. J. Inorg. Chem.*, 2021, 4543–4551.
52 Y. Gil, R. C. de Santana, A. S. S. de Camargo, L. G. Merízio, P. F. Carreño, P. Fuentealba, J. Manzur and E. Spodine, *Dalton Trans.*, 2023, **52**, 3158–3168.
53 J. Corredoira-Vázquez, C. González-Barreira, A. M. García-Deibe, J. Sanmartín-Matalobos, M. A. Hernández-Rodríguez, C. D. S. Brites, L. D. Carlos and M. Fondo, *Inorg. Chem. Front.*, 2024, **11**, 1087–1098.
54 J.-C. G. Bünzli, A.-S. Chauvin, H. K. Kim, E. Deiters and S. V. Eliseeva, *Coord. Chem. Rev.*, 2010, **254**, 2623–2633.
55 M. Hasegawa, H. Ohmagari, H. Tanaka and K. Machida, *J. Photochem. Photobiol.*, 2022, **50**, 100484.
56 L. Wu, X.-D. Huang, W. Li, X. Cao, W.-H. Fang, L.-M. Zheng, M. Dolg and X. Chen, *J. Am. Chem. Soc. Au.*, 2024, **4**, 3606–3618.
57 M. Sinchow, R. Chaicharoen, T. Chuasaard, B. Yotnoi, C. Saenjum, A. Ngamjarurojana and A. Rujiwatra, *ACS Omega*, 2024, **9**, 49441–49451.
58 B. Dutta, P. Bag, B. Adhikary, U. Flörke and K. Nag, *J. Org. Chem.*, 2004, **69**, 5419–5427.

59 J. Lisowski, *Molecules*, 2022, **27**, 4097.
60 T. Gunnlaugsson, A. J. Harte, J. P. Leonard and M. Nieuwenhuyzen, *Chem. Commun.*, 2002, 2134–2135.
61 M. Ren, Z.-L. Xu, S.-S. Bao, T.-T. Wang, Z.-H. Zheng, R. A. S. Ferreira, L.-M. Zheng and L. D. Carlos, *Dalton Trans.*, 2016, **45**, 2974–2982.
62 M. Enel, N. Leygue, S. Balayssac, S. Laurent, C. Galaup, L. Vander Elst and C. Picard, *Dalton Trans.*, 2017, **46**, 4654–4668.
63 V. R. M. Nielsen, C. H. Simms, D. Kovacs, M. F. Allen, M. J. Langton, S. Faulkner and T. J. Sørensen, *Chem. – Eur. J.*, 2025, **31**, e02305.
64 H. Yan and W.-B. Sun, *Dalton Trans.*, 2025, **54**, 17007–17024.
65 B. Drahoš, I. Císařová, O. Laguta, V. T. Santana, P. Neugebauer and R. Herchel, *Dalton Trans.*, 2020, **49**, 4425–4440.
66 P. Antal, B. Drahoš, R. Herchel and Z. Trávníček, *Inorg. Chem.*, 2016, **55**, 5957–5972.
67 P. Antal, B. Drahoš, R. Herchel and Z. Trávníček, *Dalton Trans.*, 2016, **45**, 15114–15121.
68 P. Antal, B. Drahoš, R. Herchel and Z. Trávníček, *Eur. J. Inorg. Chem.*, 2018, 4286–4297.
69 B. Drahoš, I. Šalitroš and R. Herchel, *Inorg. Chem.*, 2025, **64**, 22683–22697.
70 N. Su, J. S. Bradshaw, X. X. Zhang, P. B. Savage, K. E. Krakowiak and R. M. Izatt, *J. Heterocycl. Chem.*, 1999, **36**, 771–775.
71 D. Prętka, D. Marcinkowski, A. Siwiak, M. Kubicki, G. Consiglio, V. Patroniak and A. Gorczyński, *CrystEngComm*, 2024, **26**, 4167–4180.
72 H. Yang, Y.-X. Meng, H.-Q. Tian, D.-C. Li, S.-Y. Zeng, Y. Song and J.-M. Dou, *Dalton Trans.*, 2020, **49**, 1955–1962.
73 S. Li, S. Jansone-Popova and D.-E. Jiang, *Sci. Rep.*, 2024, **14**, 11301.
74 S. A. Cotton and J. M. Harrowfield, *Encyclopedia of Inorganic and Bioinorganic Chemistry*, 2012.
75 J. Costamagna, G. Ferraudi, B. Matsuhiro, M. Campos-Vallette, J. Canales, M. Villagrán, J. Vargas and M. J. Aguirre, *Coord. Chem. Rev.*, 2000, **196**, 125–164.
76 L. Gui, R. Huang, H. Liang, Y. Wang, W. Sun, L. Li and X. Teng, *Spectrochim. Acta A Mol. Biomol. Spectrosc.*, 2025, **339**, 126239.
77 A. K. R. Junker, L. R. Hill, A. L. Thompson, S. Faulkner and T. J. Sørensen, *Dalton Trans.*, 2018, **47**, 4794–4803.
78 O. Storm and U. Lüning, *Chem. – Eur. J.*, 2002, **8**, 793–798.
79 C. Harriswangler, B. L. McNeil, I. Brandariz-Lendoiro, F. Lucio-Martínez, L. Valencia, D. Esteban-Gómez, C. F. Ramogida and C. Platas-Iglesias, *Inorg. Chem. Front.*, 2024, **11**, 1070–1086.
80 A. F. Abdel-Magid and S. J. Mehrman, *Org. Process Res. Dev.*, 2006, **10**, 971–1031.
81 D. Prętka, D. Marcinkowski, N. Vadra, P. Woźny, M. Runowski, M. Kubicki, V. Patroniak, G. Consiglio, G. Forte and A. Gorczyński, *Inorg. Chem. Front.*, 2025, **12**, 8445–8459.
82 H. M. D. Bandara and S. C. Burdette, *Chem. Soc. Rev.*, 2012, **41**, 1809–1825.
83 C. Hillel, S. Rough, C. J. Barrett, W. J. Pietro and O. Mermut, *Commun. Chem.*, 2024, **7**, 250.